

Role of Optical Phonons in Bulk Molybdenum Diselenide Thermal Properties Probed by Advanced Raman Spectroscopy

HPSTAR
1037-2020

Zuo-Yuan Dong, Ya-Kang Peng, Hao Yu, Wei-Jian Li, Jia-Wei Hu, Chen Luo,
Xing Wu,* and Xiao-Jia Chen*

The solid-state-based thermoelectric (TE) materials have attracted considerable interest for their potential application in energy conversion. In general, high-frequency optical phonon modes are always thought to have a negligible contribution to thermal transport due to their short mean free path. Herein, the optical phonons effect in bulk molybdenum diselenide (MoSe_2) is studied using advanced low-wavenumber Raman spectroscopy with a wide temperature range. It is found that the cubic anharmonicity is dominant at low temperatures, and quartic anharmonicity becomes gradually stronger with increasing temperature. The obtained E_{2g}^1 mode is the most susceptible to the anharmonicity effect and has high phonon density of states (DOS). This is an effect that cannot be explained by previous TE models and, therefore, offers new insight into the nature of phonon transport in 2D materials. The results reveal that the thermal transport can be regulated via high-frequency phonon scattering.

1. Introduction

In recent years, transition metal dichalcogenides (TMDCs) are considered promising thermoelectric (TE) materials due to their low-dimensional properties.^[1,2] TMDCs are a family of graphene-like 2D materials with the formula of MX_2 , where M represents a transition metal element (such as Mo, W, and so on), and X refers to a chalcogen (S, Se, or Te). Unlike graphene lacking bandgap, several TMDCs prove to possess sizable bandgaps around 1–2 eV, making them suitable for use in electronic and optoelectronic devices.^[3–6] Molybdenum diselenide (MoSe_2) is one of the most studied TMDCs, and considerable device designs related to MoSe_2 have been proposed.^[7–10] TE materials can directly convert heat into electrical energy, and their

efficiency is determined by the dimensionless figure of merit ZT ($ZT = S^2\sigma T/\kappa$), where S is the Seebeck coefficient, σ is the electrical conductivity, T is the absolute temperature, and κ is the thermal conductivity.^[11] Recent reports suggested that reducing the material dimensions can increase ZT due to suppressed thermal conductivity through boundary phonon scattering.^[1,12,13] Thus, 2D materials, such as TMDCs, provide a new direction on enhancing TE performance. MoSe_2 was predicted to be a good TE material,^[14] in which low thermal conductivity is preferred. Although the thermal properties of TMDCs are different between the bulk and few-layer, the trends of temperature-dependent thermal conductivity are the same.^[15,16] It is essential to investigate

the thermal properties of bulk MoSe_2 to achieve its commercial applications.

The crystal thermal properties are governed by lattice vibrations, that is, phonon transport. Anharmonic lattice forces lead to phonon anharmonicity, and from this perspective, one phonon vibration mode can decay into two or more modes to maintain the equilibrium of energy and momentum.^[17,18] The phonon anharmonicity is critical to the thermal conductivity of crystals. In general, the thermal conductivity is primarily contributed by acoustical phonons, and little relates to optical phonons due to their short mean free path. However, when the specimen size decreases to nanoscale considering phonon scattering, optical phonons are no longer negligible.^[19,20] In recent years, many theoretical studies pointed to the importance of optical phonons on thermal transport from different perspectives. For example, Zhu and Zhang found that the optical modes remarkably suppress the thermal conductivity of diamane via selecting suitable functional groups.^[21] Lan et al. indicated that the low thermal conductivity of rare-earth pyrochlores is caused by the interference between the optical phonons and the acoustic phonons.^[22]

For experimentally studying optical phonons, Raman spectroscopy is a powerful technique with its non-invasive and non-destructive properties to samples. Raman spectrum can reflect the optical phonon frequency in the center of the crystal Brillouin zone, providing an effective way for the study of phonon scattering mechanism. Temperature-dependent Raman spectra are able to extract a phonon anharmonic scattering

Z.-Y. Dong, C. Luo, Prof. X. Wu
School of Communication and Electronic Engineering
East China Normal University
Shanghai 200241, China
E-mail: xwu@ee.ecnu.edu.cn

Z.-Y. Dong, Y.-K. Peng, H. Yu, W.-J. Li, J.-W. Hu, Prof. X.-J. Chen
Center for High Pressure Science and Technology Advanced Research
Shanghai 201203, China
E-mail: xjchen@hpstar.ac.cn

 The ORCID identification number(s) for the author(s) of this article can be found under <https://doi.org/10.1002/pssb.202000251>.

DOI: 10.1002/pssb.202000251

process from Raman shift and evolution of full-width at half-maximum (FWHM), illuminating the thermal transport behaviors in crystals. This method has been widely used to study the anharmonicity of silicon,^[23] graphene,^[24] PdS,^[25] MoS₂,^[26] WS₂,^[27] and so on. However, there is a lack of systematic research on the anharmonicity of MoSe₂ over a wide temperature range. In addition, the variation of the shear mode E_{2g}² of MoSe₂ with temperature is absent in current experimental works, which may be important to know the anharmonic effect of MoSe₂. Therefore, the systematic study on temperature-dependent Raman spectra of MoSe₂ is imminent.

In our work, an experimental study on the temperature dependence of the frequency and linewidth of MoSe₂ probed by Raman spectroscopy is performed. The temperatures widely range from 4 to 1000 K, and the wavenumber is down to 10 cm⁻¹. The phonon anharmonicity of MoSe₂ is extracted from the Raman shift and the evolution of FWHM with temperature. In addition, the phonon dispersion curves and phonon density of states (DOS) of MoSe₂ are calculated by the first-principles theory. Based on experimental data and calculated results, the phonon scattering mechanism and its influence on thermal conductivity are discussed in detail.

2. Results and Discussion

2.1. Structure and Raman Properties of MoSe₂

MoSe₂ consists of three structure polytypes according to its different symmetrical features, including 2H, 3R, and 1T. Schematic diagrams of 2H-MoSe₂ from three views are shown in Figure 1a–c, which show that the 2H type is hexagonal symmetry, possessing two Se–Mo–Se layers with a total of six atoms per unit, and the layers are connected by weak van der Waals

force with a distance of 6.5 Å.^[28] It should be noted that the MoSe₂ discussed in this article is all 2H-MoSe₂. Figure 1d is the sketch of the homemade Raman system, which can get low wavenumber Raman spectra down to 10 cm⁻¹. The incident light (the red solid line) emitted by the laser is reflected by the BragGrate notch filter (BNF) and mirror, and then focused by the lens onto the sample. The scattered light of the sample (the purple dotted line) returns to the original path and is incident on a pair of convex lens groups after BNF. A pinhole is placed in the confocal point of the convex lens to remove incident laser light from the scattered light. The scattered light then passes through a pair of BNF again to reduce Rayleigh scattered light and improve spectral quality. The BNF used in the Raman system was first reported by Tan et al. to investigate the shear mode of graphene.^[29] After that, the light is dispersed by the grating, collected by the charge-coupled devices (CCDs) finally.

The experiments on bulk MoSe₂ of Raman scattering were carried out, which can provide a reference for future research about 2D MoSe₂. Bulk MoSe₂ comprises 18 phonon vibration modes, including 3 acoustical modes and 15 optical modes. The irreducible representations of optical modes at Γ point in Brillouin zone are^[30]

$$A_{1g} + E_{1g} + 2E_{2g} + 2A_{2u} + 2E_{1u} + E_{2u} + 2B_{2g} + B_{1u} \quad (1)$$

Among them, E_{2g}², E_{1g}, A_{1g}, and E_{2g}¹ are Raman active modes, which are all observed in our Raman spectra shown in Figure 2. Figure 2a gives the evolution of Raman peaks excited with 488 nm laser with temperature from 4 to 1000 K. The upper panel of Figure 2b gives 2D presentation of temperature-dependent Raman spectra of MoSe₂, and the bottom panel shows the three typical Raman spectra at 4, 300, and 1000 K. The four first-order Raman modes E_{2g}², E_{1g}, A_{1g}, and E_{2g}¹ are 27.0, 168.4, 242.2, and 284.6 cm⁻¹ at 300 K, respectively, consistent well with

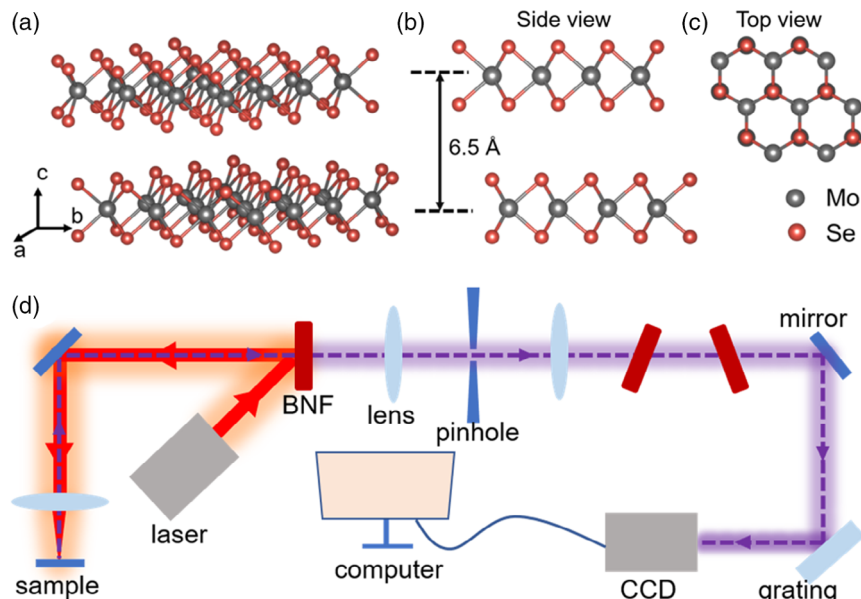


Figure 1. The schematic diagrams of MoSe₂ from the a) front view, b) side view, and c) top view. The crystallographic directions and interlayer spacing are marked. d) Sketch of the low-wavenumber Raman system. The red solid line represents incident light, and the purple dotted line indicates the scattered light. BNF is BragGrate notch filter, and CCD is charge-coupled device.

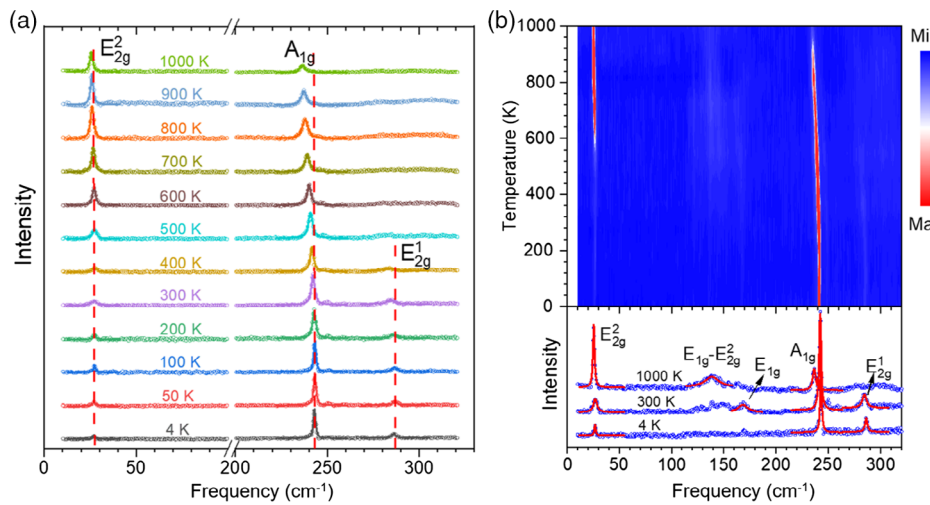


Figure 2. The Raman spectra of MoSe₂ from 4 to 1000 K and the wavenumber down to 10 cm^{-1} excited with 488 nm laser. a) The evolution of E_{2g}^2 , A_{1g} , and E_{2g}^1 modes with temperature. After 500 K, the E_{2g}^1 mode is no longer clearly visible. b) Top: 2D presentation of temperature-dependent Raman spectra. The colors from blue to red indicate the intensity of Raman peaks. Bottom: the typical Raman spectra at 4, 300, and 1000 K. The peaks are fitted using Lorentz function. All the visible modes exhibit redshift and broaden.

previous reports.^[31] The representations of Raman vibration modes of E_{2g}^2 , A_{1g} , and E_{2g}^1 are given in the insets of Figure 3a–c. We can clearly see that the E_i symmetry modes root in the lattice vibration in-plane, and the A_i modes result from the out-of-plane vibration along the *c*-axis. The low-frequency mode E_{2g}^2 is interlayer shear mode, which is rarely acquired in experiments due to the high requirements of Raman equipment. The shear mode is susceptible to the symmetry, stacking, and layer number of materials. For bulk, according to linear chain model, the shear modulus is obtained once the frequency of shear mode is detected.^[32,33] The shear mode E_{2g}^2 is observed to intensify obviously with increasing temperature, and it exhibits similar behavior under the excitation of 660 nm laser (see Figure S1, Supporting Information), which may be caused by temperature effect.^[34] The E_{2g}^1 mode becomes unclear excited with 488 nm laser at more than 500 K, which does not mean that this mode disappears. The E_{2g}^1 mode can be identified excited with 660 nm laser over 500 K (see Figure S1, Supporting Information). In addition, the second-order Raman mode $E_{1g}-E_{2g}^2$ is clearer at high temperatures owing to the enhancement of the E_{2g}^2 mode.

2.2. The Behaviors of Temperature-Dependent Frequency and Linewidth of Optical Phonons

From 4 to 1000 K, the frequencies of all observed modes show redshift, and the linewidth gets broadened. To analyze the redshift and broadened linewidth qualitatively, the evolutions of frequencies and FWHM of E_{2g}^2 , A_{1g} , and E_{2g}^1 modes with temperature are given in Figure 3. The FWHM is utilized to depict the linewidth. Figure 3a–c shows that the frequency of E_{2g}^2 mode shifts from 27.6 to 25.6 cm^{-1} , and A_{1g} mode decreases from 243.7 to 236.5 cm^{-1} with temperature from 4 to 1000 K. From 200 to 600 K, the linear change of A_{1g} mode is $-0.0074 \text{ cm}^{-1} \text{ K}^{-1}$, and the values of monolayer MoSe₂ reported in previous works are -0.0054 and $-0.012 \text{ cm}^{-1} \text{ K}^{-1}$.^[35,36] From

4 to 500 K, the frequency of E_{2g}^1 mode decreases from 287.4 to 282.5 cm^{-1} . Meanwhile, from 4 to 1000 K, the FWHM of A_{1g} mode broadens from 1.3 to 3.6 cm^{-1} , and from 4 to 500 K, the FWHM of E_{2g}^1 mode broadens from 2.8 to 12.7 cm^{-1} , which are shown in Figure 3d–f. The variation of FWHM of E_{2g}^2 with temperature exhibits irregularity, possibly caused by limitations in the resolution of the Raman system.

The temperature-dependent frequency shifts can be interpreted as the contribution of phonon anharmonic effect $\Delta\omega_A$ and thermal expansion of the lattice $\Delta\omega_E$. Hence, the temperature-dependent phonon frequency can be expressed as^[27,37]

$$\omega(T) = \omega_0 + \Delta\omega_A(T) + \Delta\omega_E(T) \quad (2)$$

in which $\Delta\omega_E(T)$ can be written as

$$\Delta\omega_E(T) = \omega_0 \exp\left(-\gamma \int_0^T \alpha dT\right) - \omega_0 \quad (3)$$

where T is the Kelvin temperature, ω_0 is the intrinsic frequencies of optical phonons at $T=0 \text{ K}$, γ is the Grüneisen parameter, and α is the thermal expansion coefficient. Ding et al. calculated the mode Grüneisen parameters and the thermal expansion coefficient of bulk MoSe₂ using the first-principles theory. We extracted the Grüneisen parameters of E_{2g}^2 , A_{1g} , and E_{2g}^1 modes are 1.33, 0.35, and 0.38, respectively. The thermal expansion coefficient is $2.7 \times 10^{-5} \text{ K}^{-1}$ when temperature is above 200 K.^[38] According to the calculation results, the product of Grüneisen parameter and thermal expansion coefficient can be regarded as a constant from 0 to 1000 K. Thermal expansion is vital to temperature-dependent Raman shifts, and the similar studies on thermal expansion were also discussed in other works.^[39–41]

According to Klemens model, in anharmonic interaction, the optical phonon can decay into two or three lower energy phonons. Considering the difference of phonon energy in decaying, it can be expressed as^[17,23]

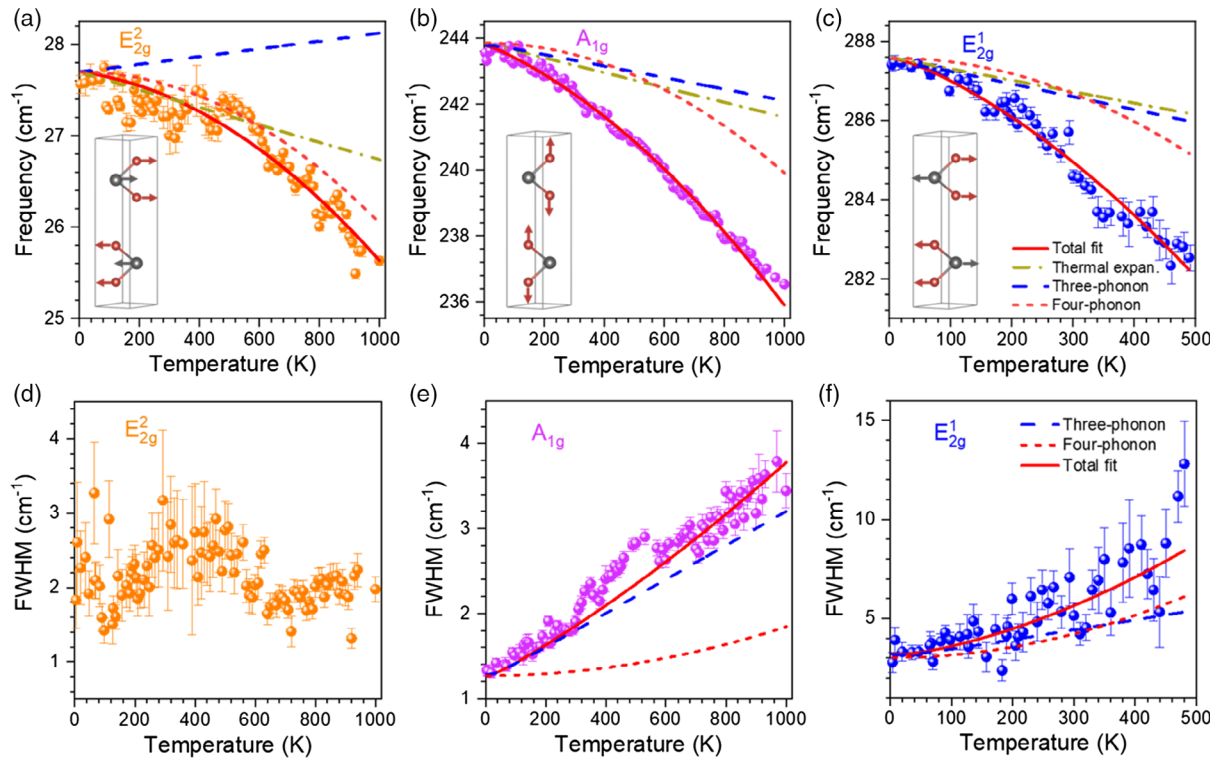


Figure 3. a–c) The frequency and d–f) the FWHM of E_{2g}^2 , A_{1g} , and E_{2g}^1 modes versus temperature. The corresponding modes are marked in the sub-figures. The blue and red dashed lines represent the theoretical fitting according to three- and four-phonon anharmonic processes, respectively. The yellow dashed-dotted line represents the contribution of thermal expansion. The red solid line is total fitting. The insets of (a–c) give the diagrams of corresponding Raman active vibration modes.

$$\Delta\omega_A(T) = A \left[1 + \sum_{m=1}^2 \frac{1}{e^{\hbar\omega_m/k_B T} - 1} \right] + B \left[1 + \sum_{n=1}^3 \left(\frac{1}{e^{\hbar\omega_n/k_B T} - 1} + \frac{1}{(e^{\hbar\omega_n/k_B T} - 1)^2} \right) \right] \quad (4)$$

where the second and third terms represent cubic and quartic anharmonic processes, respectively. In the equation, \hbar is the reduced Planck constant, and k_B is the Boltzmann constant. A and B are cubic and quartic anharmonic coefficients, which are related to three- and four-phonon scattering processes, respectively. ω_m ($m = 1, 2$) and ω_n ($n = 1, 2, 3$) are the frequencies of decaying phonons, satisfying $\omega_0 = \omega_1 + \omega_2$ and $\omega_0 = \omega_1 + \omega_2 + \omega_3$ in three- and four-phonon processes, respectively. The Klemens model assumes that one optical phonon decays into acoustic phonons with average frequencies $\omega_1 = \omega_2 = \omega_0/2$ for the cubic process and $\omega_1 = \omega_2 = \omega_3 = \omega_0/3$ for the quartic process.^[17] It is reasonable to deal with the anharmonicity of MoSe₂ in this way on the basis of the phonon dispersion and DOS shown in Figure 4a. Based on Equation (2)–(4), the experimental data of frequencies shifts with temperature are fitted, as shown in Figure 3. The yellow dashed-dotted line indicates the contribution of thermal expansion. The blue and red dashed lines represent the three- and four-phonon anharmonic processes, respectively. The red solid line is total fitting. For all the three modes, thermal expansion has a non-negligible effect on Raman shifts. Meanwhile, the nonlinear changes in frequency

are mainly caused by anharmonicity. At low temperatures, the trend of fitting curves is mainly influenced by the thermal expansion and three-phonon anharmonic process. As the temperature rises, the quartic anharmonic effect increases, and the final frequencies are determined by the thermal expansion, three-phonon, and four-phonon processes together. It is noticed that the cubic anharmonic coefficient of the E_{2g}^2 mode is positive, and its quartic coefficient is negative, which are determined by the magnitudes and signs of the anharmonic terms in the interatomic potential.^[41] The cubic and quartic anharmonic coefficients are extracted and listed in Table 1. The anharmonic coefficient of the E_{2g}^1 mode over a wider temperature range is obtained with the help of 660 nm laser (see Figure S2, Supporting Information). It shows that the cubic and quartic anharmonic coefficients of the E_{2g}^1 mode are -0.3 and -0.0071 , respectively. Only by three-phonon processes and thermal expansion fitting, the anharmonic coefficients are also extracted (see Figure S3 and Table S1, Supporting Information). The result of the fitting is worse than considering the four-phonon process. All the results show that the anharmonic coefficient of the E_{2g}^1 mode is the largest, which indicates that the anharmonic effect of E_{2g}^1 is the strongest.

The following is focused on a Raman mode linewidth analysis. In the case of ideal harmonicity, the linewidth of Raman peaks is infinitesimally narrow, but in reality, the peaks always display a certain linewidth. The cause of this result can be divided into the influences of impurities Γ_i and anharmonic scattering process Γ_a in crystal, and thus, we can get^[42]

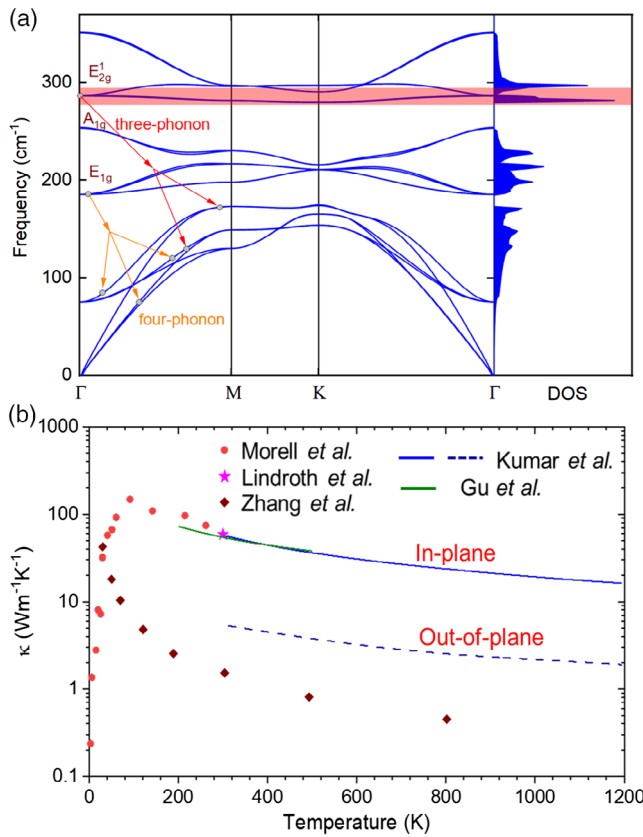


Figure 4. a) The phonon dispersion curves and DOS of MoSe₂. The red shaded area indicates the DOS near E_{2g}¹ mode. The three- and four-phonon process diagrams are marked on the curves. b) Temperature-dependent change in in-plane and out-of-plane thermal conductivities of MoSe₂ from previous works.^[14,15,43–45]

Table 1. Cubic and quartic anharmonic coefficients of MoSe₂.

Mode	A [cm ⁻¹]	B [cm ⁻¹]	C [cm ⁻¹]	D [cm ⁻¹]
E _{2g} ²	0.0027 ± 0.00072	-0.000024 ± 0.000027	-	-
A _{1g}	-0.077 ± 0.011	-0.0045 ± 0.00033	0.088 ± 0.0019	0.00066 ± 0.00004
E _{2g} ¹	-0.17 ± 0.06	-0.016 ± 0.0039	0.26 ± 0.07	0.021 ± 0.005

$$\Gamma = \Gamma_i + \Gamma_a \quad (5)$$

where Γ represents the FWHM of Raman peaks. Due to the high-quality single crystal MoSe₂, the first term Γ_i is not considered. Consequently, anharmonic phonon scattering plays a dominant role in the broadening. In general, the FWHM gets broadened, as the temperature increases on account of the enhancement of anharmonic effect. According to an anharmonic model, the evolution of FWHM with temperature can be expressed as^[23]

$$\begin{aligned} \Gamma(T) = \Gamma_0 + C & \left[1 + \sum_{m=1}^2 \frac{1}{e^{\hbar\omega_m/k_B T} - 1} \right] \\ & + D \left[1 + \sum_{n=1}^3 \left(\frac{1}{e^{\hbar\omega_n/k_B T} - 1} + \frac{1}{(e^{\hbar\omega_n/k_B T} - 1)^2} \right) \right] \end{aligned} \quad (6)$$

where Γ_0 is the FWHM at $T = 0$ K, and C and D are the anharmonic coefficients. The values of ω_m and ω_n are consistent with them in Equation (4).

Using Equation (6), the variations of FWHM of MoSe₂ with temperature are fitted, which are exhibited in Figure 4. Due to the irregularity of the E_{2g}² mode, it was not fitted. The constants C as well as D are extracted and summarized in Table 1, unveiling the contribution of three- and four-phonon processes to FWHM. From Table 1, the constants C are 0.088 and 0.26 cm⁻¹ for A_{1g} and E_{2g}¹ modes, respectively. The constants D are 0.00066 and 0.021 cm⁻¹ for A_{1g} and E_{2g}¹ modes, respectively. These results demonstrate that the anharmonic effect of E_{2g}¹ mode is stronger than A_{1g}, which is consistent with the results of the above-mentioned frequencies anharmonicity (the coefficients A and B).

2.3. Analysis of Anharmonic Influence on Thermal Conductivity

The anharmonic effect has a great influence on the thermal conductivity of the crystal, especially in the high-temperature range. In general, the total thermal conductivity originates from the lattice vibration and electric transport. Due to the low electrical conductivity of MoSe₂, thermal conductivity is mainly contributed by the lattice vibration, that is, phonon transport. Thus, we focus entirely on the lattice contribution κ_l , which follows the formula $\kappa_l = 1/3 cv^2\tau$, where c is the lattice specific heat capacity, v is the phonon group velocity, and τ is the phonon lifetime. Among them, the phonon lifetime can be expressed as

$$\tau \propto \frac{1}{\Gamma} \quad (7)$$

Therefore, the anharmonic effect can effectively reduce the phonon group velocity, thereby reducing the lattice thermal conductivity. To further understand the effect of phonon anharmonicity on thermal conductivity, the previous works on thermal conductivity of MoSe₂ are given in Figure 4b.^[14,15,43–45] At low temperatures, thermal conductivity rapidly rises to a maximum value with increasing temperature, yet after about 100 K, it begins to drop slowly. The anharmonic effect can well account for this phenomenon. At low temperatures, the phonon anharmonic effect is weak, and thermal conductivity is mainly determined by the lattice specific heat capacity, which is subject to the relationship of $c \propto T^3$. In high-temperature regions, the lattice specific heat capacity no longer changes with temperature. As the number of phonons increases to participate in thermal transport, phonon anharmonic scattering plays a dominant role in the evolution of thermal conductivity with temperature. Even though the main contribution to thermal conductivity is acoustical phonons, according to related researches, optical phonons contribute more than 20% at the nanoscale and can no longer be ignored.^[19,20] In our results about MoSe₂, the anharmonicity of E_{2g}¹ optical mode is strongest. In addition, from the calculated phonon dispersion curves and DOS of MoSe₂ shown in Figure 4, one can see that the DOS is highest near E_{2g}¹ mode. This shows that the thermal conductivity of MoSe₂ is very likely to be affected by high-frequency acoustic branches such as E_{2g}¹ mode, through the interaction between optical and acoustical phonons.

3. Conclusion

In conclusion, a home-made low wavenumber Raman experimental study on temperature-dependent Raman spectra of 2D molybdenum diselenide was performed. The temperature ranges from 4 to 1000 K with low wavenumber down to 10 cm⁻¹. The temperature-dependent Raman shift is determined jointly by thermal expansion and anharmonicity. For the A_{1g} and E_{2g}¹ modes, the cubic anharmonicity is predominant at low temperatures, whereas quartic anharmonicity become stronger with the increasing temperature. For the E_{2g}² mode, it shows a little correlation with anharmonicity. Phonon dispersion curves and DOS of MoSe₂ were calculated, and it is found that the high optical branches possess high DOS. It reveals that the thermal conductivity is related to optical phonons through the interaction between optical and acoustical phonons. The effect of high-frequency optical phonons is non-negligible.

4. Experimental Section

Experimental Detail: High-quality bulk MoSe₂ was purchased from HQ Graphene. A 50 μm × 50 μm × 10 μm sample was used for in situ variable temperature Raman experiment. The sample was placed in a cryogenic chamber with flowing liquid helium for measurement from 4 to 300 K. Platinum resistance sensor was used for detecting real-time temperatures with a precision of ±0.5 K. For the high-temperature range (300–1000 K), the sample was placed on a sealed heating stage and continuous flowing of argon prevented it from being oxidized. A K-type thermocouple was used to measure the temperatures with a precision of ±1 K. The 488 nm exciting laser with a power of 2 mW was focused on the new exfoliated surface of MoSe₂ to obtain better Raman spectra. The scattered light passed through 1800 g mm⁻¹ grating and then recorded with a Princeton CCD.

Method of Calculation: Phonon dispersion calculations are performed in the framework of density functional theory and density functional perturbation theory, as implemented in the Quantum Espresso package.^[46] We used the Perdew–Burke–Ernzerhof revised for solids (PBEsol)^[47,48] and optimized norm-conserving Vanderbilt (ONCV) full-relativistic pseudopotentials.^[49,50] We choose and the plane-wave basis expansion was set to 520 eV, with a k-point grid taken as 8 × 8 × 8. The spin-orbit coupling is considered during all the calculations.

Supporting Information

Supporting Information is available from the Wiley Online Library or from the author.

Acknowledgements

This work was supported by the NSFC under grant No. 61574060, Projects of Science and Technology Commission of Shanghai Municipality Grant Nos. (19ZR1473800), Shanghai Rising-Star Program (17QA1401400), Young Elite Scientists Sponsorship Program by CAST (YESS), the Program for Professor of Special Appointment (Eastern Scholar), and the Fundamental Research Funds for the Central Universities.

Conflict of Interest

The authors declare no conflict of interest.

Keywords

low-wavenumber technique, molybdenum diselenide, Raman spectroscopy, thermal properties, thermoelectric materials

Received: April 30, 2020

Revised: May 17, 2020

Published online: June 15, 2020

- [1] D. Li, Y. Gong, Y. Chen, J. Lin, Q. Khan, Y. Zhang, Y. Li, H. Zhang, H. Xie, *Nano-Micro Lett.* **2020**, *12*, 36.
- [2] G. Zhang, Y.-W. Zhang, *J. Mater. Chem. C* **2017**, *5*, 7684.
- [3] J. Wang, J. Han, X. Chen, X. Wang, *InfoMat* **2019**, *1*, 33.
- [4] G. Rao, X. Wang, Y. Wang, P. Wangyang, C. Yan, J. Chu, L. Xue, C. Gong, J. Huang, J. Xiong, Y. Li, *InfoMat* **2019**, *1*, 272.
- [5] Q. H. Wang, K. Kalantar-Zadeh, A. Kis, J. N. Coleman, M. S. Strano, *Nat. Nanotechnol.* **2012**, *7*, 699.
- [6] J. Zhang, Y. Yu, P. Wang, C. Luo, X. Wu, Z. Sun, J. Wang, W. D. Hu, G. Shen, *InfoMat* **2019**, *1*, 85.
- [7] J.-S. Rhyee, J. Kwon, P. Dak, J. H. Kim, S. M. Kim, J. Park, Y. K. Hong, W. G. Song, I. Omkaram, M. A. Alam, S. Kim, *Adv. Mater.* **2016**, *28*, 2316.
- [8] X. Chen, X. Chen, Y. Han, C. Su, M. Zeng, N. Hu, Y. Su, Z. Zhou, H. Wei, Z. Yang, *Nanotechnology* **2019**, *30*, 445503.
- [9] A. Abderrahmane, P. J. Ko, T. V. Thu, S. Ishizawa, T. Takamura, A. Sandhu, *Nanotechnology* **2014**, *25*, 365202.
- [10] X. Wang, C. Liu, Y. Chen, G. Wu, X. Yan, H. Huang, P. Wang, B. Tian, Z. Hong, Y. Wang, S. Sun, H. Shen, T. Lin, W. Hu, M. Tang, P. Zhou, J. Wang, J. Sun, X. Meng, J. Chu, Z. Li, *2D Mater.* **2017**, *4*, 025036.
- [11] L. E. Bell, *Science* **2008**, *321*, 1457.
- [12] M. S. Dresselhaus, G. Chen, M. Y. Tang, R. G. Yang, H. Lee, D. Z. Wang, Z. F. Ren, J. P. Fleurial, P. Gogna, *Adv. Mater.* **2007**, *19*, 1043.
- [13] Z. Dong, H. Xu, F. Liang, C. Luo, C. Wang, Z.-Y. Cao, X.-J. Chen, J. Zhang, X. Wu, *Molecules* **2019**, *24*, 88.
- [14] S. Kumar, U. Schwingenschlögl, *Chem. Mater.* **2015**, *27*, 1278.
- [15] D. O. Lindroth, P. Erhart, *Phys. Rev. B* **2016**, *94*, 115205.
- [16] A. N. Gandi, U. Schwingenschlögl, *Europhys. Lett.* **2016**, *113*, 36002.
- [17] P. G. Klemens, *Phys. Rev.* **1966**, *148*, 845.
- [18] T. R. Hart, R. L. Aggarwal, B. Lax, *Phys. Rev. B* **1970**, *1*, 638.
- [19] Z. Tian, K. Esfarjani, J. Shiomi, A. S. Henry, G. Chen, *Appl. Phys. Lett.* **2011**, *99*, 053122.
- [20] M. Kazan, S. Pereira, J. Coutinho, M. R. Correia, P. Masri, *Appl. Phys. Lett.* **2008**, *92*, 211903.
- [21] L. Zhu, T. Zhang, *Appl. Phys. Lett.* **2019**, *115*, 151904.
- [22] G. Lan, B. Ouyang, J. Song, *Acta Mater.* **2015**, *91*, 304.
- [23] M. Balkanski, R. F. Wallis, E. Haro, *Phys. Rev. B* **1983**, *28*, 1928.
- [24] N. Bonini, R. Rao, A. M. Rao, N. Marzari, J. Menéndez, *Phys. Status Solidi B* **2008**, *245*, 2149.
- [25] L.-C. Chen, Z.-Y. Cao, H. Yu, B.-B. Jiang, L. Su, X. Shi, L.-D. Chen, X.-J. Chen, *Appl. Phys. Lett.* **2018**, *113*, 022105.
- [26] Z.-Y. Cao, X.-J. Chen, *Appl. Phys. Lett.* **2019**, *114*, 052102.
- [27] Y.-K. Peng, Z.-Y. Cao, L.-C. Chen, N. Dai, Y. Sun, X.-J. Chen, *J. Phys. Chem. C* **2019**, *123*, 25509.
- [28] Y. Zhang, T. R. Chang, B. Zhou, Y. T. Cui, H. Yan, Z. Liu, F. Schmitt, J. Lee, R. Moore, Y. Chen, H. Lin, H. T. Jeng, S. K. Mo, Z. Hussain, A. Bansil, Z. X. Shen, *Nat. Nanotechnol.* **2014**, *9*, 111.
- [29] P. H. Tan, W. P. Han, W. J. Zhao, Z. H. Wu, K. Chang, H. Wang, Y. F. Wang, N. Bonini, N. Marzari, N. Pugno, G. Savini, A. Lombardo, A. C. Ferrari, *Nat. Mater.* **2012**, *11*, 294.
- [30] X. Zhang, X. F. Qiao, W. Shi, J. B. Wu, D. S. Jiang, P. H. Tan, *Chem. Soc. Rev.* **2015**, *44*, 2757.

- [31] S. V. Bhatt, M. P. Deshpande, V. Sathe, R. Rao, S. H. Chaki, *J. Raman Spectrosc.* **2014**, *45*, 971.
- [32] X. Zhang, Q.-H. Tan, J.-B. Wu, W. Shi, P.-H. Tan, *Nanoscale* **2016**, *8*, 6435.
- [33] L. Liang, J. Zhang, B. G. Sumpter, Q.-H. Tan, P.-H. Tan, V. Meunier, *ACS Nano* **2017**, *11*, 11777.
- [34] T. Fujiyama, *Bull. Chem. Soc. Jpn.* **1973**, *46*, 87.
- [35] M. Yang, X. Cheng, Y. Li, Y. Ren, M. Liu, Z. Qi, *Appl. Phys. Lett.* **2017**, *110*, 093108.
- [36] D. J. Late, S. N. Shirodkar, U. V. Waghmare, V. P. Dravid, C. N. R. Rao, *ChemPhysChem* **2014**, *15*, 1592.
- [37] L. Su, Y. Zhang, Y. Yu, L. Cao, *Nanoscale* **2014**, *6*, 4920.
- [38] Y. Ding, B. Xiao, *RSC Adv.* **2015**, *5*, 18391.
- [39] X. Huang, Y. Gao, T. Yang, W. Ren, H.-M. Cheng, T. Lai, *Sci. Rep.* **2016**, *6*, 32236.
- [40] S. Najmaei, P. M. Ajayan, J. Lou, *Nanoscale* **2013**, *5*, 9758.
- [41] Z. Zhao, J. Elwood, M. A. Carpenter, *J. Phys. Chem. C* **2015**, *119*, 23094.
- [42] M. Millot, R. Tena-Zaera, V. Munoz-Sanjose, J.-M. Broto, J. Gonzalez, *Appl. Phys. Lett.* **2010**, *96*, 152103.
- [43] N. Morell, S. Tepsic, A. Reserbat-Plantey, A. Cepellotti, M. Manca, I. Epstein, A. Isacsson, X. Marie, F. Mauri, A. Bachtold, *Nano Lett.* **2019**, *19*, 3143.
- [44] X. Zhang, D. Sun, Y. Li, G. H. Lee, X. Cui, D. Chenet, Y. You, T. F. Heinz, J. C. Hone, *ACS Appl. Mater. Interfaces* **2015**, *7*, 25923.
- [45] X. Gu, R. Yang, *Appl. Phys. Lett.* **2014**, *105*, 131903.
- [46] P. Giannozzi, S. Baroni, N. Bonini, M. Calandra, R. Car, C. Cavazzoni, D. Ceresoli, G. L. Chiarotti, M. Cococcioni, I. Dabo, A. Dal Corso, S. de Gironcoli, S. Fabris, G. Fratesi, R. Gebauer, U. Gerstmann, C. Gougoussis, A. Kokalj, M. Lazzeri, L. Martin-Samos, N. Marzari, F. Mauri, R. Mazzarello, S. Paolini, A. Pasquarello, L. Paulatto, C. Sbraccia, S. Scandolo, G. Sclauzero, A. P. Seitsonen, A. Smogunov, P. Umari, R. M. Wentzcovitch, *J. Phys.: Condens. Matter* **2009**, *21*, 395502.
- [47] J. P. Perdew, K. Burke, M. Ernzerhof, *Phys. Rev. Lett.* **1996**, *77*, 3865.
- [48] J. P. Perdew, A. Ruzsinszky, G. I. Csonka, O. A. Vydrov, G. E. Scuseria, L. A. Constantin, X. Zhou, K. Burke, *Phys. Rev. Lett.* **2008**, *100*, 136406.
- [49] M. J. van Setten, M. Giantomassi, E. Bousquet, M. J. Verstraete, D. R. Hamann, X. Gonze, G. M. Rignanese, *Comput. Phys. Commun.* **2018**, *226*, 39.
- [50] D. R. Hamann, *Phys. Rev. B* **2013**, *88*, 085117.